Diurnal Variation in Martian Dust Devil Activity

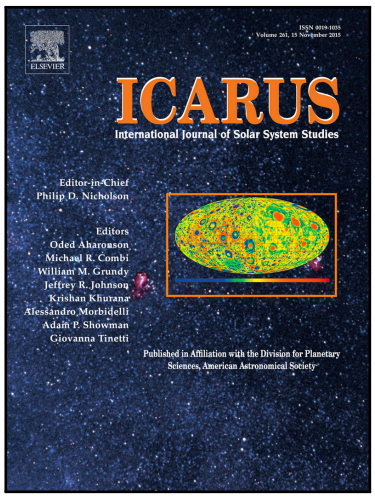

Diurnal Variation in Martian Dust Devil Activity

R.M. Chapman, S.R. Lewis, M. Balme, L.J. Steele

PII: S0019-1035(16)30289-5
DOI: 10.1016/j.icarus.2017.01.003
Reference: YICAR 12325

To appear in: *Icarus*

Received date: 15 June 2016
Revised date: 4 January 2017
Accepted date: 4 January 2017

Please cite this article as: R.M. Chapman, S.R. Lewis, M. Balme, L.J. Steele, Diurnal Variation in Martian Dust Devil Activity, *Icarus* (2017), doi: 10.1016/j.icarus.2017.01.003

Highlights

- Modelled Martian dust devil activity occurs earlier in the sol than expected.
- Peak dust devil activity occurs during morning hours across multiple areas.
- Dust devil diurnal variability is governed by local wind speeds.
- Model results show good match to surface observations of dust devil timings.
- Dust devil parameterisation in Mars Global Circulation Models is incomplete.

Diurnal Variation in Martian Dust Devil Activity

R. M. Chapman[a,*], S. R. Lewis[a], M. Balme[a], L. J. Steele[a]

[a] *The Open University, Walton Hall, Milton Keynes, MK7 6AA, UK*

Abstract

We show that the dust devil parameterisation in use in most Mars Global Circulation Models (MGCMs) results in an unexpectedly high level of dust devil activity during morning hours.

Prior expectations of the diurnal variation of Martian dust devils are based mainly upon the observed behaviour of terrestrial dust devils: i.e. that the majority occur during the afternoon. We instead find that large areas of the Martian surface experience dust devil activity during the morning in our MGCM, and that many locations experience a peak in dust devil activity before mid-sol.

We find that the diurnal variation in dust devil activity is governed by near-surface wind speeds. Within the range of daylight hours, higher wind speeds tend to produce higher levels of dust devil activity, rather than the activity simply being governed by the availability of heat at the planet's surface, which peaks in early afternoon.

Evidence for whether the phenomenon we observe is real or an artefact of the parameterisation is inconclusive. We compare our results with surface-based observations of Martian dust devil timings and obtain a good match with the majority of surveys. We do not find a good match with orbital observations, which identify a diurnal distribution more closely matching that of terrestrial dust devils, but orbital observations have limited temporal coverage, biased towards the early afternoon.

We propose that the generally accepted description of dust devil behaviour on Mars is incomplete, and that theories of dust devil formation may need to be modified specifically for the Martian environment. Further surveys of dust devil observations are required to support any such modifications. These surveys should include both surface and orbital observations, and the range of observations must encompass the full diurnal period and consider the wider meteorological context surrounding the observations.

Keywords: Mars, atmosphere, Mars, climate, Mars, surface

1. Introduction

Dust is present within the atmosphere of Mars as a constant background haze (Pollack et al., 1977; Martin, 1986; Smith et al., 2001). Martian dust devils were first identified in Viking Orbiter images (Thomas and Gierasch, 1985) and have since been observed

*Corresponding author

Email address: rhian.chapman@open.ac.uk (R. M. Chapman)

in a large number of images captured by Mars orbiting spacecraft (Fisher et al., 2005; Stanzel et al., 2006), as well as in multiple images returned from rovers on the surface (Ferri et al., 2003; Greeley et al., 2006). The tracks left behind by the passage of dust devils – usually visible as dark streaks against the higher albedo surface – have also been observed in many orbiter images (Cantor et al., 2006).

Martian dust devils are named after the apparently similar features observed on Earth. These are near-surface atmospheric vortices that are visible due to the particles they lift from the ground and entrain in a vertical, upwardly-spiraling column of air. The core of a dust devil is commonly at a lower pressure than the surrounding vortex (Sinclair, 1964). Dust devils are able to lift surface dust particles due to the wind shear stress present within the walls of the vortex (Balme et al., 2003a). The lower central pressure within the column may also contribute to dust lifting by providing an upwards force that assists the shear stress in overcoming interparticle cohesion forces (Greeley et al., 2003; Balme and Hagermann, 2006). Dust devil activity on Mars is highly variable between regions and seasons (Fisher et al., 2005), and Martian dust devils are more frequently observed in local spring and summer months (Thomas and Gierasch, 1985; Balme et al., 2003b; Cantor et al., 2006).

This work uses a Martian Global Circulation Model (MGCM) to investigate the diurnal variation in Martian dust devil activity. The rate of surface dust lifting by dust devils (henceforth termed "dust devil lifting") was used as a proxy for assessing the level of dust devil activity at any specific location and time. No statements can made about the number or size of dust devils represented by a specific level of activity.

In Section 2 we discuss the model parameterisation that simulates dust devils in the Martian atmosphere; in Section 3 we present the results from the model; in Section 4 we explore in detail the components of the dust devil parameterisation and consider how our results compare against orbital and surface observations. Section 5 summarises this work and in Section 6 we detail our conclusions.

2. Method

The MGCM used in this work (henceforth referred to as "the MGCM") is a global, multi-level spectral model of the Martian atmosphere up to an altitude of ∼100 km, as described by Forget et al. (1999). Simulations were completed at a resolution of 5° latitude × 5° longitude, resulting in a gridbox at the equator measuring ∼300 × 300 km.

Each simulation begins with a two-year 'spin-up' period from a dynamically static atmosphere, in order to allow the annual progression of tracer distributions to settle into representative cycles. The results analysed below correspond to the third full Mars Year (MY) of each simulation, starting at solar longitude $L_S = 0°$. The prescribed atmospheric dust loadings used within these simulations correspond to daily global dust maps described by Montabone et al. (2015), which were obtained by binning and interpolation of spacecraft data. The Martian calendar adopted herein follows the approach proposed within Clancy et al. (2000). Following Lewis et al. (1999), a Martian 'hour' is 1/24th of a sol (a sol being a Martian day). All times herein that refer to surface-level phenomena relate to local times.

The dust devil parameterisation was implemented by Newman et al. (2002). The subroutine was modified by Mulholland (2012) to add a two-moment tracer scheme, but

the core of the parameterisation remained the same. Here, we outline the components of this dust devil parameterisation; in Section 4, we assess in detail the impact of each component on the diurnal timing of dust devil lifting.

The flux of surface dust lifted by dust devils within an MGCM gridbox, F_{devil}, is calculated from the sensible heat flux, F_s, and the dust devil thermodynamic efficiency, η:

$$F_{\mathrm{devil}} = \alpha_D \eta F_s \tag{1}$$

where α_D is a tuneable parameter representing the 'dust devil lifting efficiency', required due to the uncertainty surrounding the actual quantity of dust that Martian dust devils are able to lift. The value of this parameter is set such that the total annual dust cycle within a simulation best matches the range of observed dust opacities (Newman et al., 2002). For the current resolution, $\alpha_D = 1.13333 \times 10^{-8}$ kg J^{-1}. This value is constant throughout the simulation.

The quantity η arises from the modelling of a dust devil as a 'heat engine', following Rennó et al. (1998). η is the thermodynamic efficiency of a dust devil: the fraction of the input heat that is converted into mechanical work. This thermodynamic efficiency is approximated as $\eta \approx 1 - b$, where

$$b = \frac{(p_{\mathrm{surf}}^{\chi+1} - p_{\mathrm{top}}^{\chi+1})}{(p_{\mathrm{surf}} - p_{\mathrm{top}})(\chi + 1)p_{\mathrm{surf}}^{\chi}} \tag{2}$$

in which p_{surf} is the local surface pressure, p_{top} is the pressure at the top of the convective boundary layer (CBL) within the Martian atmosphere, and χ is equal to the specific gas constant (R) divided by the specific heat capacity at constant pressure (c_p).

The sensible heat flux, F_s, represents the input heat available to drive the dust devil 'heat engine', and can be written as:

$$F_s = \rho c_p C_D U (t_{\mathrm{surf}} - t_{\mathrm{atm}}) \tag{3}$$

where ρ is the near-surface atmospheric density, C_D is the surface drag coefficient, U is the horizontal wind speed, t_{surf} is the surface temperature, and t_{atm} is the temperature in the lowest layer of the atmosphere.

The surface drag coefficient C_D is parameterised using the classical expression for a boundary layer drag coefficient (Esau, 2004):

$$C_D = \left(\frac{\kappa}{\ln(1 + z/z_0)} \right)^2 \tag{4}$$

where the von Kármán constant $\kappa \approx 0.4$, z is the height of the lowest layer of the atmosphere, and z_0 is the surface roughness length. In these simulations $z \sim 5$ m. The surface roughness length was kept constant at $z_0 = 0.01$ m, resulting in a constant value of C_D across the planet's surface.

The wind speed U is the magnitude of the near-surface wind speed, calculated from the large-scale zonal and meridional wind components (u and v) within the lowest layer of the atmosphere.

The dust devil parameterisation in operation within the MGCM has been used as the basis for similar parameterisations in other Mars atmospheric models. The NASA Ames

Mars General Circulation Model (GCM) directly incorporates the Newman et al. (2002) parameterisation (Kahre et al., 2006, 2008), as does the Geophysical Fluid Dynamics Laboratory (GFDL) Mars GCM parameterisation (Basu et al., 2004).

Surface dust was also lifted into the atmosphere through lifting by near-surface wind stress, implemented within the MGCM following Newman et al. (2002) as modified by Mulholland et al. (2013). Lifting by near-surface wind stress is thought to be the primary dust lifting process associated with Martian dust storms (e.g. Strausberg et al. (2005), Basu et al. (2006) and Wilson (2011)).

To provide comparison and validation datasets for the model results we have chosen to use observations of Martian dust devils obtained from orbit and from the surface. Global plots and histograms from the model output can be compared with orbital observations; localised plots of model results can be compared with surface observations.

The gridboxes chosen for the localised analysis correlate as closely as possible with the locations of Mars landers identified in Table 1. The daily cycle of dust devil lifting was plotted for each location, taking into account the time of year and the local atmospheric dust environment of the observations.

The simulations were completed using prescribed dust fields. In the current approach, dust lifted by both dust devils and near-surface wind stress is combined into a total atmospheric dust field, which is then scaled (at gridbox resolution) to match daily global maps of the optical depth of the Martian atmosphere (Montabone et al., 2015). Dust from both surface-level processes is treated as equivalent once it is within the atmosphere. The local atmospheric dust environment during a lander's observations can be approximated using these fields: the modelled optical depth that would be reported at a surface location in the vicinity of a lander's position can be compared to the optical depth recorded by that lander during its observations.

If a dust map has been constructed for the year in which a mission took place (for example, the Phoenix mission landed in MY29), a simulation using the relevant atmospheric dust loading was used for the comparison analysis. For missions that took place before the earliest dust map observation (MY24, beginning in July 1998), the local optical depth observed by the lander was compared with the local optical depth produced by the MGCM simulations across multiple Mars years of differing atmospheric dust conditions, and results from the closest match were then used for the analysis. Dust maps are available from MY24 to MY32.

The amount of dust present in the atmosphere has an effect on dust devil lifting primarily through its impact on surface and near-surface temperatures. Atmospheric dust absorbs incident solar radiation, resulting in a heating of the atmosphere and a reduction of surface insolation (Zurek, 1978). A high level of atmospheric dust, such as that observed during dust storms, will therefore cause an increase in near-surface atmospheric temperatures and a decrease in insolation-driven surface temperatures. This reduces the surface-to-atmosphere temperature gradient ($(t_{\mathrm{surf}} - t_{\mathrm{atm}})$ in Equation 3), which lowers the amount of surface-level heat available to drive dust devil formation.

3. Results

From our simulation results we created global maps of the diurnal variation in dust devil lifting. For each gridbox, dust devil lifting was calculated at 12 local times, spaced

Lander	Lander location (latitude/°N, longitude/°E)
Viking Lander 2 (VL2)	47.97, 134.25
Pathfinder	19.33, 33.55
Phoenix	68.22, 125.70
MER Spirit	-14.61, 175.47
MSL Curiosity	-4.59, 137.44

Table 1: Locations of NASA landers, Mars Exploration Rover (MER) Spirit and Mars Science Laboratory (MSL) Curiosity.

evenly through a sol. Dust devil lifting is somewhat stochastic in nature, varying from sol to sol in both amplitude and timing, so to investigate trends, simulation results were averaged over 30° L_S-long sections of the Martian year. This allows the identification of the time-of-sol at which dust devils are most commonly active within a given gridbox during the analysed portion of the year: the 'peak dust devil lifting' time. (To eliminate extremely low levels of dust devil lifting from subsequent calculations, a threshold dust lifting rate was applied at this stage of the analysis. This threshold was set at 1×10^{-11} kg m^{-2} s^{-1}, a value chosen by considering the dust lifting rates at the lander sites, see Figures 4 and 5.)

An example of these global maps is shown in Figure 1, which displays the range of timings in the daily peak dust devil lifting across the planet's surface. This figure displays data from the start of the Martian year (L_S = 0-30°), corresponding to early Northern Hemisphere spring. Figure 2a shows the same data plotted as a histogram. These figures identify a clear bimodal distribution of the diurnal timing of peak dust devil lifting, with one peak evident in the mid-morning and one peak evident in the late afternoon.

The global diurnal variation of dust devil lifting changes through the year, displaying a seasonal shift from a bimodal to unimodal distribution. Figure 2b displays a histogram of data from the same simulation, but at a point in the year approaching perihelion, corresponding to late Northern Hemisphere autumn (L_S = 210-240°). This figure displays a unimodal timing distribution of peak dust devil lifting, with a single peak in the mid-afternoon. Figure 3 shows histograms of all 12 such 30° L_S-long sections of the Martian year, illustrating the seasonal shift in the distribution.

Surface observations provide more dust devil lifting diurnal variation information than orbital observations. We completed simulations for direct comparison with previous studies that use data from the four surface missions identified in Table 1. The comparisons presented here for each landing site correspond to the times of year analysed by the previous studies. For the shorter duration missions, Pathfinder and Phoenix, those studies covered the full length of the mission; for VL2 and Spirit, those studies covered only a portion of the whole mission.

It should be noted that the majority of lander data reported within the comparison studies are pressure detections of atmospheric vortices, with one study reporting directly imaged dust devils (detailed in Section 4.2). The two data types are not completely equivalent: although all dust devils are vortices, not all vortices entrain dust.

The following figures display the diurnal variation in dust devil lifting for each site. The envelope encompassing all of the results obtained through the analysed time period

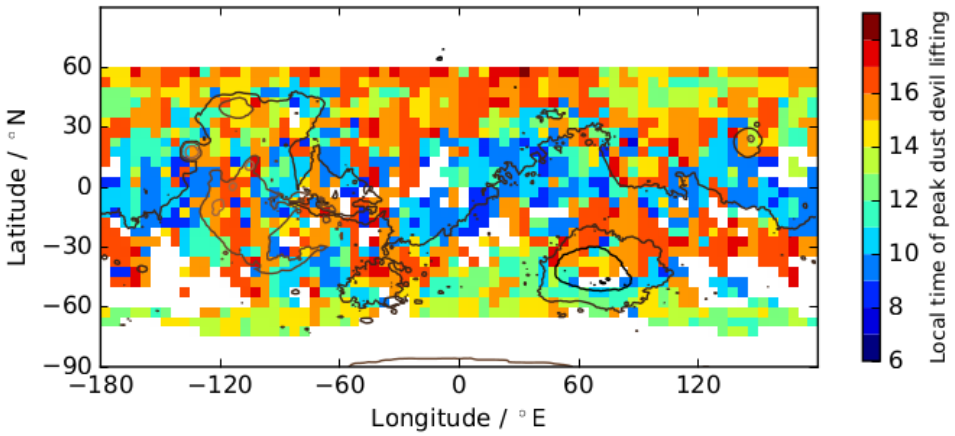

Figure 1: Global plot in which colour scale denotes the diurnal timing of peak dust devil lifting across the Martian surface. The data displayed here represent dust devil lifting averaged across L_S = 0-30°, from a simulation using a relatively low atmospheric dust loading. Gridboxes coloured yellow, orange or red relate to afternoon peaks in dust devil lifting; blue gridboxes relate to morning peaks in dust devil lifting. White gridboxes indicate no lifting or below threshold lifting. Contour lines denoting topography are included for illustration only.

is shown, as well as the average across that period. Note that the amounts of dust lifted vary by two orders of magnitude between the different lander sites.

The Viking Landers reached Mars during MY12, a year that experienced large dust storms and subsequent high atmospheric dust loading. The visible optical depth observed at the VL2 landing site during the earliest portion of the mission (L_S = 117-148°) was reported as ∼0.3-0.4 (Pollack et al., 1977; Colburn et al., 1989). This is best matched by the visible optical depth simulated in this region at this time of year in the MGCM simulation using the MY25 dust field (MY25 also experienced a large dust storm later in the year). Figure 4a shows analysed dust devil lifting in the vicinity of the VL2 landing site, alongside data from the comparison study by Ringrose et al. (2003). The Pathfinder mission took place during MY23, L_S = 140-190°. The visible optical depth observed by the lander varied from ∼0.4 shortly after landing to ∼0.6 towards the end of the mission (Smith and Lemmon, 1999). The MGCM simulation using the MY28 dust field produces a visible optical depth of ∼0.5 in this region throughout the length of the mission. Figure 4b shows analysed dust devil lifting in the vicinity of the Pathfinder landing site, alongside data from the comparison study by Murphy and Nelli (2002). The Phoenix mission landed in MY29, operating through L_S = 77-148°. Figure 4c shows analysed dust devil lifting in the vicinity of the Pathfinder landing site, alongside data from the comparison study by Ellehoj et al. (2010). The long duration of the MER Spirit mission enabled extended observations of dust devils, encompassing multiple years. The annual dust devil 'season' observed by the rover spanned the second half of the year, L_S ∼ 175-355°. Three full dust devil seasons were observed by Spirit in the relevant comparison study, spanning MY27-MY29. Figure 5 shows analysed dust devil lifting in the vicinity of the Spirit operational site, alongside data from the comparison study by Greeley et al. (2010). MSL Curiosity landed in MY31, beginning its ongoing mission on

$L_S = 150°$. Figure 4d shows analysed dust devil lifting in the vicinity of the Curiosity site through the first full year (668 sols) of the rover's operation, alongside data from the comparison study by Kahanpää et al. (2016).

4. Discussion

Analogies are often drawn between dust devils on Mars and on Earth, primarily due to the lack of *in situ* measurements of Martian dust devil characteristics. Terrestrial dust devil activity has been observed to peak in the afternoon: Sinclair (1969) described dust devil observations in Arizona spanning 1000 to 1630 and reaching a maximum between 1300 and 1400; Snow and McClelland (1990) observed dust devils in New Mexico starting

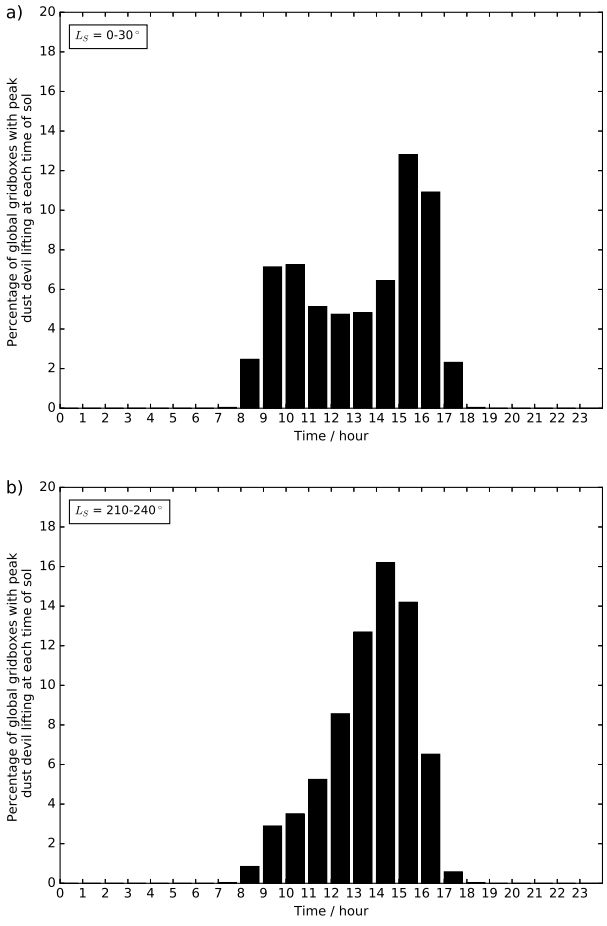

Figure 2: Histograms displaying the diurnal timing of peak dust devil lifting as a percentage of all surface gridboxes. a) Dust devil lifting averaged across L_S = 0-30° (identical data displayed in Figure 1): a clear bimodal curve can be seen in the data, with a morning peak between 0900 and 1100 and an afternoon peak between 1500 and 1700. b) Dust devil lifting averaged across L_S = 210-240°: the unimodal curve peaks between 1400 and 1500.

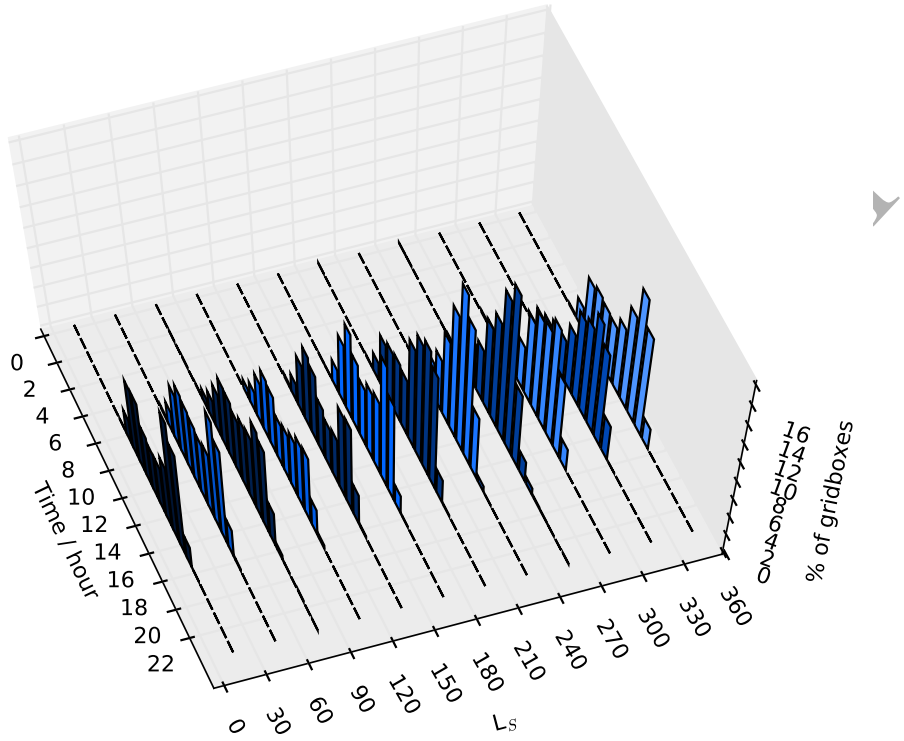

Figure 3: Histogram displaying the diurnal timing of peak dust devil lifting as a percentage of all surface gridboxes. These results show data through a full Martian year, averaged across sections covering 30° L_S. The bimodal distribution in peak dust devil lifting timing is visible for the sections covering L_S = 0-210° (Northern Hemisphere spring and summer), while the sections plotted L_S = 210-330° (Northern Hemisphere autumn and winter) display a unimodal distribution. The shape of the section covering L_S = 330-360° suggests a returning shift to a bimodal distribution.

around 1100, peaking in number between 1230 and 1300, and ending by 1600; Oke et al. (2007) reported dust devil observations in New South Wales, Australia, occurring between 1120 and 1740, with activity peaking between 1400 and 1540; and Lorenz and Lanagan (2014) used pressure data to identify dust devil events in Nevada starting around 0900, peaking twice in the afternoon (shortly before 1400 and around 1600) and lasting until 2000.

While Figure 1 shows gridboxes across the surface of Mars displaying peaks in dust devil lifting during both the morning and the afternoon, Figure 6 shows in more detail that some individual gridboxes display morning-only dust devil lifting, some display afternoon-only dust devil lifting, and others display more extended dust devil lifting through the course of the sol, including occasional bimodal lifting.

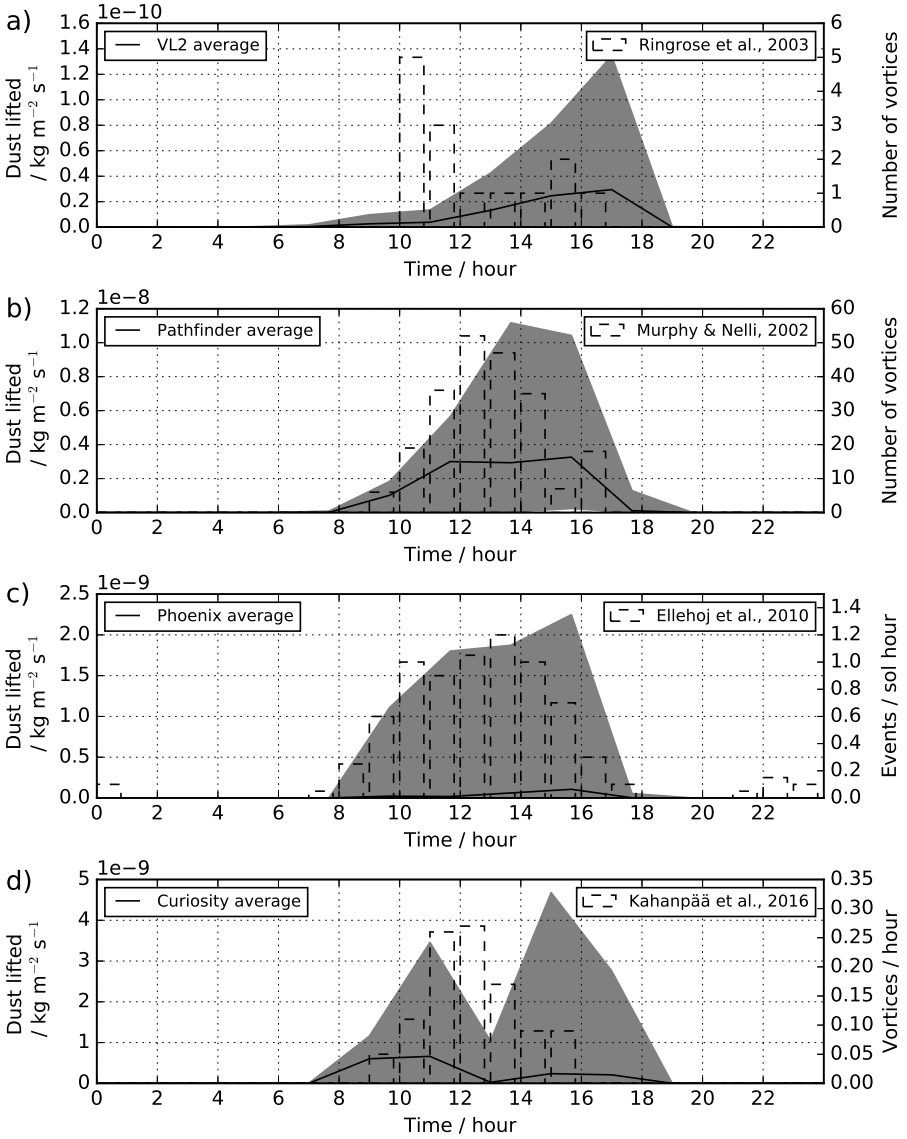

Figure 4: Hourly dust devil lifting in the vicinity of three lander sites, plotted against the left vertical axes. For each site, the average is displayed as a black solid line, and the grey shading is the envelope of all results produced during the relevant time period. Plotted against the right vertical axes are data from the comparison studies. a) VL2 landing site, L_S = 117-148°, plotted against data from Ringrose et al. (2003); b) Pathfinder landing site, L_S = 140-190°, plotted against data from Murphy and Nelli (2002); c) Phoenix landing site, L_S = 77-148°, plotted against data from Ellehoj et al. (2010); d) MSL Curiosity site, L_S = 157° MY31 to L_S =157° MY32, plotted against data from Kahanpää et al. (2016).

4.1. Diurnal variability within the dust devil parameterisation

The root of the timing variability in peak dust devil lifting can be found by examining the component variables within Equation 1. The values of α_D, c_p, and C_D were constant

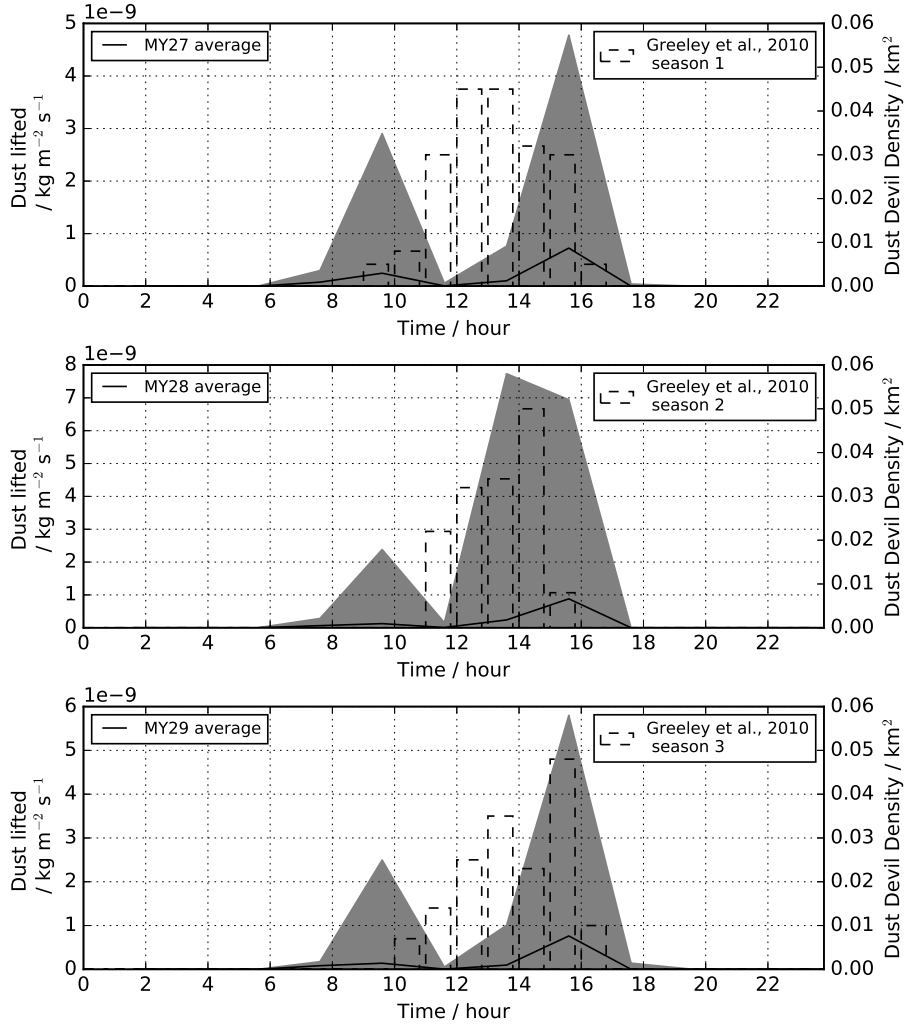

Figure 5: Hourly dust devil lifting in the vicinity of the MER Spirit site across the three Mars years considered, plotted against the left vertical axes. Each average (black solid line) is displayed, and the grey shading encompasses all results produced during the time periods (each L_S = 170-359°). Plotted against the right vertical axes are data from the comparison study by Greeley et al. (2010).

during this simulation, so cannot in themselves cause the diurnal variation displayed in the dust devil lifting. We now describe the diurnal variations of the thermodynamic efficiency η, the near-surface atmospheric density ρ, and the surface-to-atmosphere temperature gradient, $(t_{\mathrm{surf}} - t_{\mathrm{atm}})$.

The diurnal variation of η follows the diurnal variation of the depth of the CBL. The depth of the CBL, represented by $p_{\mathrm{surf}} - p_{\mathrm{top}}$, is driven directly by the increase of heat in the lower portion of the atmosphere, arising from insolation-driven heating of both the surface and the near-surface atmosphere (Spiga et al., 2010). As such, the depth of

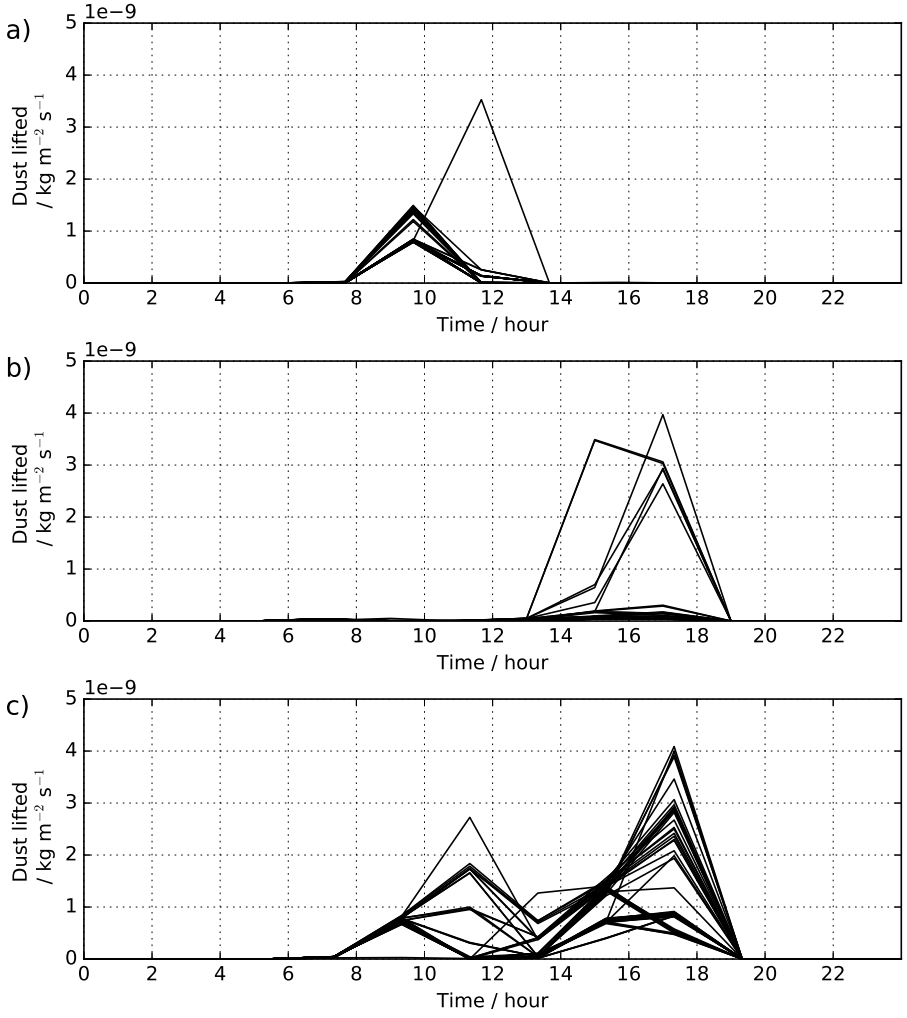

Figure 6: Dust devil lifting within individual gridboxes through L_S = 120-150°; this time of year was chosen as an example period. Each plotted line corresponds to the dust devil lifting through one sol (60 sols in total). The plots show varying diurnal timings of dust devil lifting: a) morning-only dust devil lifting (gridbox centred on -12.5°N, 175°E), b) afternoon-only dust devil lifting (37.5°N, 75°E), and c) through-sol dust devil lifting, displaying a nominal bimodal distribution (27.5°N, -10°E).

the CBL follows the diurnal pattern of heating in the lowest levels of the atmosphere: CBL depth steadily increases during the morning, reaches a peak in the late afternoon, and decreases (more rapidly) in the evening. While the local absolute depth of the CBL varies greatly over the planet depending on local surface height (Hinson et al., 2008), the diurnal pattern of the CBL depth is consistent due to its dependence on insolation. The value of η will therefore peak in late afternoon, its local value determined by the local depth of the CBL; a CBL depth of $\sim$5 km results in η $\sim$0.06 and a CBL depth of $\sim$8 km results in η $\sim$0.08 (where $\chi = 0.256793$).

Figure 7 shows example η curves calculated for an equatorial location (the gridbox centred on -2.5°N, -5°E, which is the landing site of MER Opportunity) at around $L_S \approx 245°$, in a year experiencing a low atmospheric dust loading (MY24). It can be seen that the example curve of η increases during the morning, reaches a maximum shortly after peak insolation, and then decays more quickly in the evening.

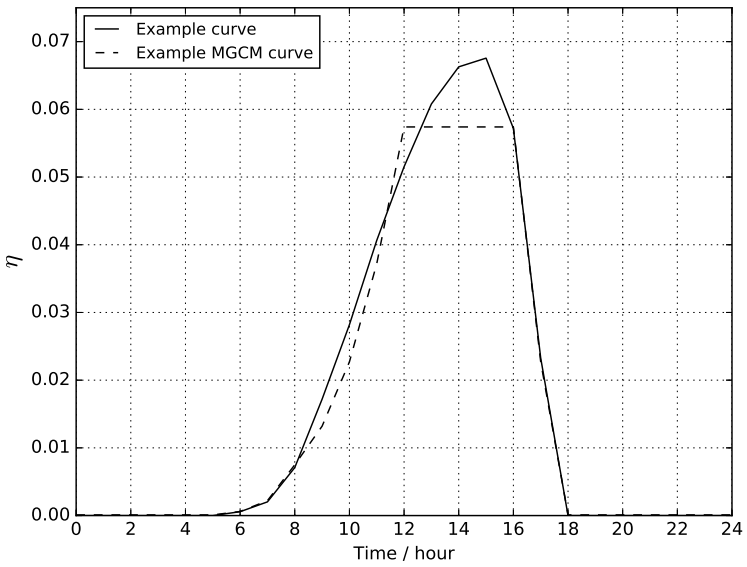

Figure 7: The example η curve (solid line) was calculated using a representative diurnal CBL depth curve extracted from the Mars Climate Database (Lewis et al., 1999). The example MGCM η curve (dashed line) illustrates how the calculation of η within the model can be affected by the discretisation of atmospheric layers. This truncation/quantisation effect is due to the depth of the model's atmospheric layers, which are shallow close to the surface (only tens of metres deep in the lowest layers) but increase in depth as altitude increases (~2000 m deep at an altitude of 5 km).

Near-surface atmospheric density, ρ, varies widely by location, driven by local variation in the near-surface atmospheric pressure. Atmospheric density curves from surface locations at extremes of altitude are plotted in Figure 8. Although the absolute values plotted are substantially different, the diurnal variation in near-surface density is similar in both locations.

The temperature gradient between the surface and the near-surface atmosphere, $(t_{\mathrm{surf}} - t_{\mathrm{atm}})$, has a predictable diurnal cycle, the magnitude of which is dependent on latitude and time of year. Surface temperature peaks at maximum insolation, around 1300 local time, while near-surface atmospheric temperature peaks between 1600 and 1700. This lag between the temperature curves produces a maximum in $(t_{\mathrm{surf}} - t_{\mathrm{atm}})$ that occurs slightly earlier in the sol than the peak surface temperature. Although surface and near-surface temperatures vary by a large amount with changing latitude and altitude, the timings of the peaks in the temperature curves remain relatively consistent. Figure 9 displays the temperature curves associated with a gridbox in the region of Meridiani Planum.

As η, ρ, and $(t_{\mathrm{surf}} - t_{\mathrm{atm}})$ follow smooth, predictable diurnal patterns, these variables

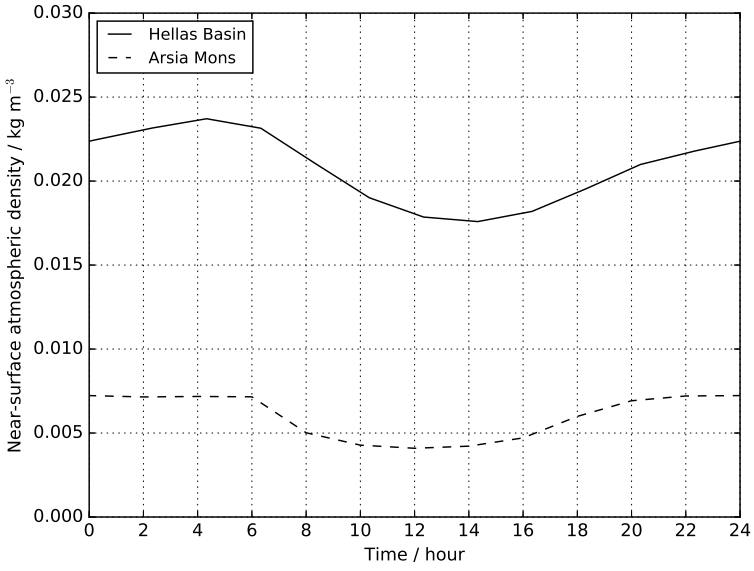

Figure 8: Near-surface atmospheric density at two locations: within Hellas basin (at an altitude ∼6.7 km below Mars datum) and in the vicinity of Arsia Mons (at an altitude ∼15.5 km above Mars datum). Values are averaged over L_S = 240-270°. The shape of the diurnal curve is similar for both sites through the length of a sol.

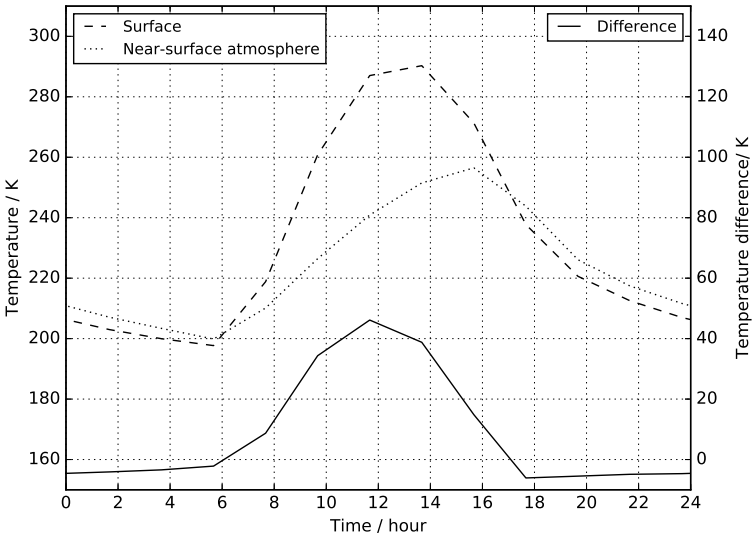

Figure 9: Surface temperature and near-surface atmospheric temperature curves plotted against the left axis; temperature difference ($t_{\mathrm{surf}} - t_{\mathrm{atm}}$) plotted against the right axis. Values are averaged over L_S=240-270°, this gridbox is centred on -2.5°N, -5°E. The peak in temperature difference occurs around 1200, leading the peak in surface temperature.

provide no insight into the short-term variability of dust devil lifting. Both η and $(t_{\mathrm{surf}} - t_{\mathrm{atm}})$ must be greater than zero for any dust devil lifting to occur, but their through-sol variation follows predictable diurnal patterns. The only component in Equation 1 that does not follow a smooth, predictable curve through each sol is the near-surface wind speed U. This variable is calculated from the zonal and meridional wind components of the large scale winds within the lowest model layer of the atmosphere (typically at a height of ∼5 m above the surface), and can be highly variable throughout the course of one sol. Figure 10 shows an example of the variability present in near-surface wind speed. Dust devil lifting within the same gridbox is also shown: in this particular gridbox the timing of the dust devil lifting is broadly distributed through daylight hours. Figure 11 shows the near-surface wind speeds associated with the examples of morning-only and afternoon-only dust devil lifting plotted in Figure 6.

Figure 12 shows histograms of the diurnal timing of peak near-surface wind speeds through the course of a simulated Martian year. A seasonal shift is evident, moving between a bimodal distribution of timings (during Northern Hemisphere spring and summer) and a unimodal distribution (during Northern Hemisphere autumn and winter). This pattern closely matches the distributions identified in diurnal timings of peak dust devil lifting (see Figure 3).

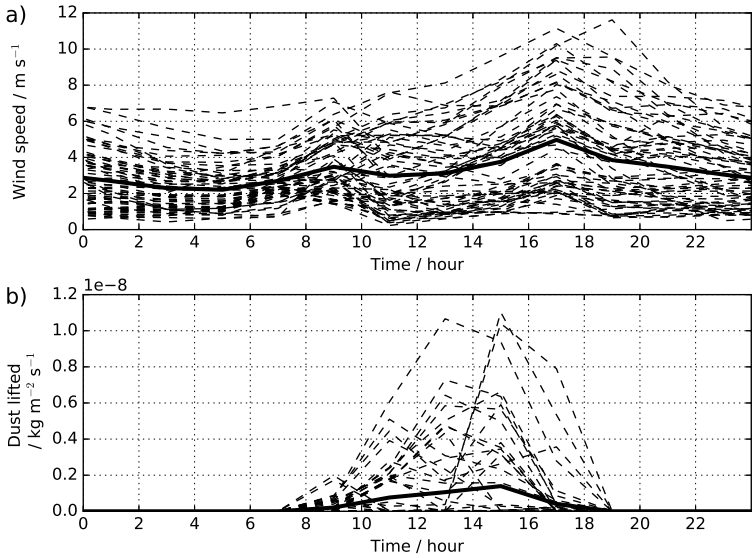

Figure 10: Near-surface wind speeds and dust devil lifting within an individual gridbox (47.5°N, 135°E) through the period L_S = 0-30°. Each dashed line corresponds to values through one sol (60 sols in total), the heavy solid line shows the average of this period. Both panels show the variability of the plotted values: a) wide variation in the amplitude of wind speeds, b) variation in the timing and amplitude of dust devil lifting.)

From the discussion above it can be concluded that the variability in the timing of dust devil lifting depends primarily on the speed of the near-surface wind. Insolation is the root driver of Martian dust devil formation: the period of the sol in which there is a positive value of sensible heat at the planet's surface provides an envelope of time

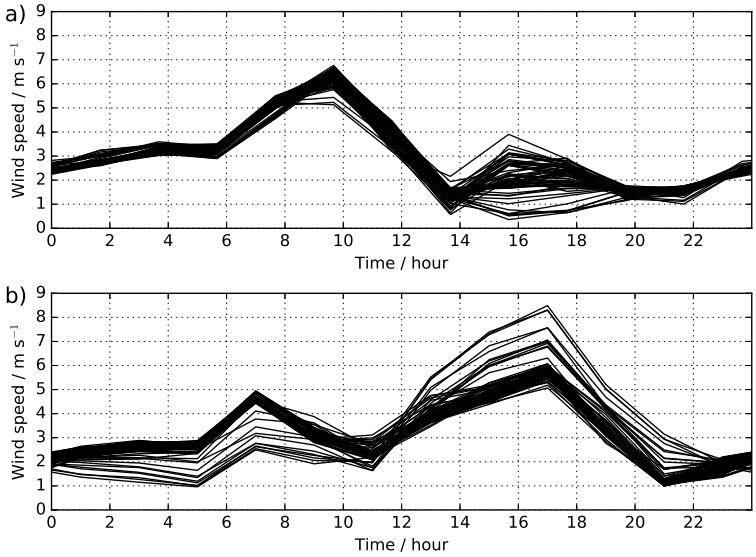

Figure 11: Near-surface wind speeds within individual gridboxes through the period L_S = 120-150°. Each plotted line corresponds to the varying wind speed through one sol (60 sols in total). a) gridbox centred on -12.5°N, 175°E, b) gridbox centred on 37.5°N, 75°E. Compare with panels a) and b) in Figure 6.

during which dust devils *can* form. Precisely *when* dust devils form within that timing envelope is governed by the instantaneous near-surface wind speed, at least, as described in the dust devil parameterisation schemes used in MGCMs. Figure 13 shows how the wind speed and temperature terms of the parameterisation vary globally, and highlights examples of the correlation between these terms and the resultant level of dust devil lifting.

The magnitude and direction of the near-surface wind flow arises from a complex interaction of local and large scale influences. Solar heating of the atmosphere drives global diurnal thermal tides, the smaller-scale flow of which is affected by more local variations in surface properties (Wilson and Hamilton, 1996). Variations in topography give rise to slope winds (upslope during daylight hours and downslope during the night), and contrasts in surface thermal properties (such as variations in albedo and thermal inertia, or polar ice cap edges) have a changing effect on the flow of local-scale winds throughout the diurnal heating cycle (Read and Lewis, 2004). Interactions between these locally-forced wind flows and large-scale, regional circulations (e.g. lower-level Hadley circulation) must also be considered (Toigo and Richardson, 2003).

Observations of terrestrial dust devil activity suggest that near-surface winds must be present for the initiation of dust devils, but that high wind speeds may inhibit their formation: Sinclair (1969) observed dust devil activity decreasing as wind speeds increased; Oke et al. (2007) observed dust devils only when ambient wind speeds were between 1.5 and 7.5 m s^{-1}; Kurgansky et al. (2010) observed an increase in dust devil numbers when wind speeds were between 2 and 8 m s^{-1}. It has been proposed that terrestrial convective vortices forming in high wind conditions will be rapidly destroyed by a shearing of the

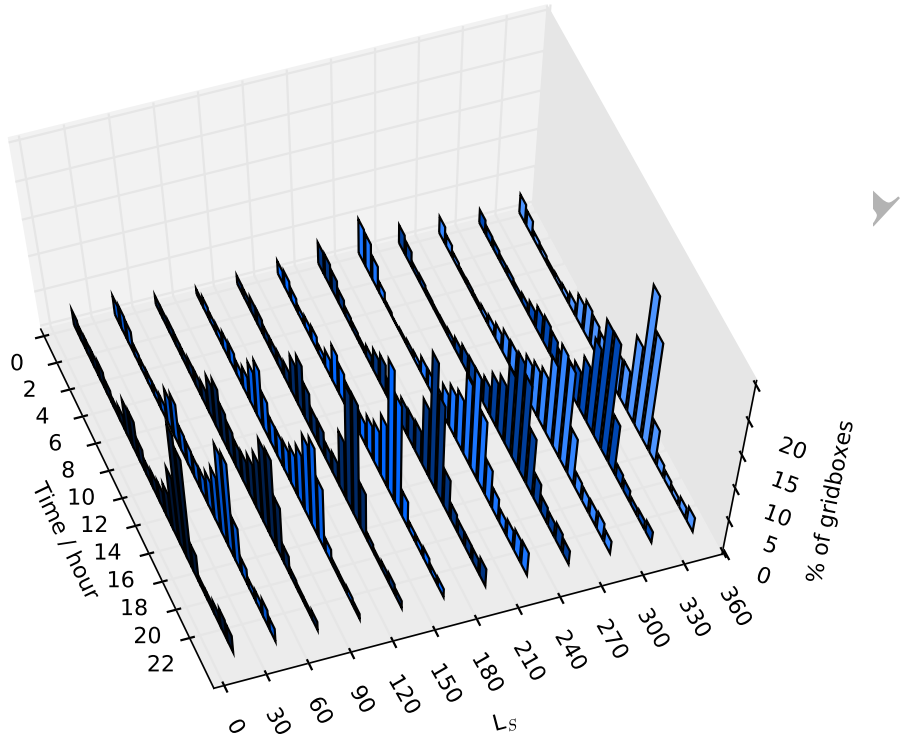

Figure 12: Histogram displaying the diurnal timing of peak near-surface wind speeds as a percentage of all surface gridboxes. A bimodal distribution in timings is evident in the sections covering L_S = 0-210° while the sections plotted L_S = 210-300° display a unimodal distribution. The shape of the sections through L_S = 300-360° suggest a returning shift to a bimodal distribution. Compare with the similar annual variation in peak dust devil lifting timings in Figure 3.

upper portion of the vortex from the lower portion due to the wind speeds present (Oke et al., 2007), and analyses of terrestrial dust devil populations have found that favourable conditions for dust devil formation can be modelled using increasing wind speeds to curb the level of dust devil activity (Lyons et al., 2008; Jemmett-Smith et al., 2015). Conversely, Toigo et al. (2003) completed high resolution numerical simulations of Martian dust devils, in which dust devils formed in 'no wind' and 'high wind' scenarios but did not form in low or medium wind scenarios, potentially highlighting another incidence in which terrestrial dust devil theory cannot be directly applied to the Martian phenomena.

Some dust devils on Mars have been identified moving considerably faster than terrestrial dust devils. Martian dust devils have been observed to travel in the direction of the ambient wind (Stanzel et al., 2008; Reiss et al., 2014), with horizontal speeds of 27 m s^{-1} identified from surface observations (Greeley et al., 2010), and up to 59 m s^{-1} calculated from orbital images (Stanzel et al., 2008). Limited data is available on Martian near-surface wind speeds (Balme et al., 2012), but if there is a systematic inhibition of Martian dust devil formation due to high wind speeds, it occurs at much higher speeds

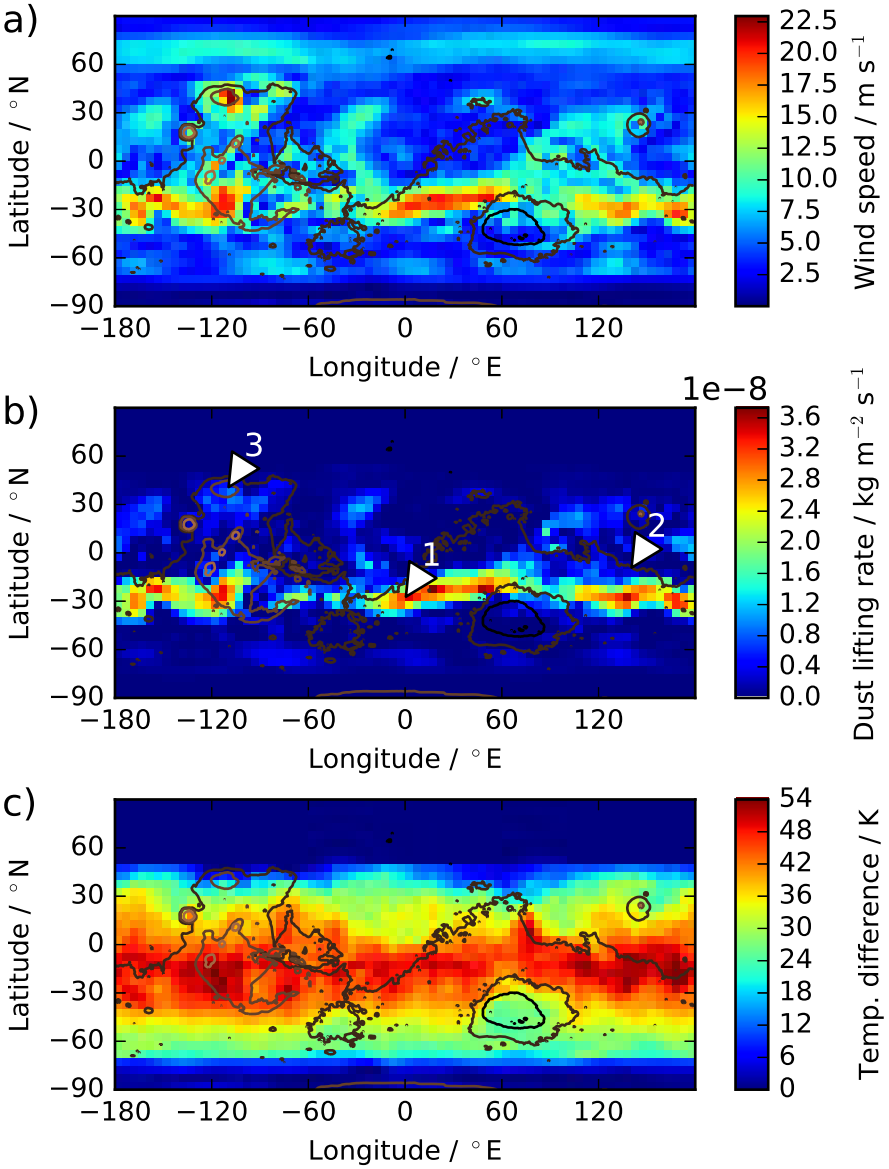

Figure 13: Global map of a) near-surface wind speeds, b) dust devil lifting and c) surface-atmosphere temperature difference, ($t_{\mathrm{surf}} - t_{\mathrm{atm}}$). All gridboxes are displayed at a local time of 1300, providing a global picture of activity at one specific time of sol. Values are averaged over L_S = 240-270°. Dust devil lifting occurs within the 'permitted' envelope represented by ($t_{\mathrm{surf}} - t_{\mathrm{atm}}$) > 0, but at specific locations governed by the wind speeds. Compare the locations labelled in panel b): 1. -28°N, 0°E (high temperature difference, high winds, high lifting), 2. -10°N, 140°E (high temperature difference, low winds, low lifting), 3. 40°N, -110°E (low temperature difference, high winds, low lifting).

than those proposed for terrestrial dust devils.

4.2. Comparisons with observations

We can compare our global results with observations of global Martian dust devil activity, although there have been limited surveys of dust devil diurnal variation using orbital observations. It should be noted, however, that the total number of dust devils observed in orbital images is necessarily limited by the resolution of those images. Mars landers and rovers have observed many small dust devils that could not currently be seen from space (Stanzel et al., 2006).

Some dust devil surveys are temporally constrained by the viewing angle provided by the platform: for example, surveys using Mars Global Surveyor (MGS) Mars Orbital Camera (MOC) images are restricted to a local time of 1300-1500 (Cantor et al., 2006). Stanzel et al. (2008) used an observation set that was not so temporally restricted to survey dust devils and their characteristics: Mars Express High Resolution Stereo Camera (HRSC) images. All seasons of the year were included in their image survey, and the regions selected for scrutiny were identified as 'active dust devil areas' in previous studies; they found a strong peak in dust devil numbers between 1400 and 1500, with a smaller peak between 1200 and 1300. The morning peak in dust devil lifting evident in our results was not identified by this survey, in which dust devils were only observed in images captured after 1100. HRSC images span 0600 to 2000.

We compare our results directly with results from the comparison studies mentioned in Section 3 (and displayed in Figures 4 and 5). The comparisons are detailed below and summarised in Table 2.

Ringrose et al. (2003) identified 38 convective vortices in pressure data from the first 60 sols of the Viking Lander 2 mission. The anticipated afternoon peak was seen, although in the early afternoon (1300-1330) rather than the mid-afternoon. A morning peak was also evident, between 1000 and 1030. The authors commented on this morning peak, proposing that it was due to convective vortices produced by the local wind interacting with the body of the lander, rather than 'naturally generated' dust devils. In contrast to that study, our averaged results for this location show a strong peak in dust devil lifting during the late afternoon, around 1700 (Figure 4a). Our results show limited dust devil lifting in the morning, although lifting does still occur ahead of the afternoon peak. Due to the suggestion by Ringrose et al. (2003) that at least some of the observed morning vortices were likely false positives, potentially excluding up to four of the nine morning observations, we have described the match between the observations and our results as a 'partial match' in Table 2.

Murphy and Nelli (2002) used pressure data from the full length of the Pathfinder mission (L_S = 142-183°) to identify 79 pressure signatures indicative of atmospheric vortices passing over or near the lander. Maximum vortex activity was observed between 1200 and 1300. Our averaged results for this location show afternoon dust devil lifting intensity that is relatively constant between 1200 and 1600, with a slight dip in activity around 1400 (Figure 4b). However, the full envelope of our results displays a distribution similar in shape to the distribution observed by Murphy and Nelli (2002), although it is shifted later in the sol by approximately one hour.

Ellehoj et al. (2010) considered data from the whole length of the Phoenix mission and identified 502 "probable" convective vortices from drops in pressure data. The analysis

of these vortices is split by the authors into vortices identified between L_S = 77-111° and vortices identified between L_S = 111-148°, due to their observation that the 'dust devil season' at the lander location began around L_S = 111°. The vortex observations through L_S = 77-111° peak around 1200. The vortex observations through the dust devil season of L_S = 111-148° display a double peak: a morning peak around 1100 and an afternoon peak around 1300. The authors propose that the number of vortices actually peaks around 1200 through the latter period as well, and that this apparent bimodal curve is due to a repeated ∼30 minute gap in observations around mid-sol: the period at which the lander paused operations every sol in order to complete data transfer. Our averaged results for this location show extremely low levels of dust devil lifting that peak around 1600 (Figure 4c). This low average is due to the fact that an extended section of our L_S = 77-111° period does not containing any dust devil lifting at all. The increase in observed devil activity identified by Ellehoj et al. (2010) as the local start of the dust devil season does not occur in our results until $L_S \approx 144°$. The majority of the dust devil lifting results displayed in Figure 4c are from the period L_S = 144-148°. Although therefore covering a limited period of time, the diurnal distribution of these results is quite similar in shape and timing to the distribution observed by Ellehoj et al. (2010), albeit with a sharp spike around 1600 that is missing from the observed data.

Greeley et al. (2010) used images captured by the Spirit rover during three dust devil seasons, each of which started at a similar time of year ($L_S \approx 181°$). More dust devils were observed in the first dust devil season than in the following two seasons (respectively 502, 101 and 127 dust devils). The number of images taken during the latter two seasons was limited due to power considerations, and observations were either truncated (by a local dust storm in the second season) or inhibited by the rover being in less favourable locations for viewing and imaging dust devils. With regards to the time-of-sol for peak dust devil activity, results from this multi-year survey are mixed (Figure 5). Dust devil season 1 shows a broad peak of 'dust devil density' between 1200 and 1400, season 2 has a sharper peak between 1400 and 1500, and season 3 shows a small peak between 1300 and 1400 and a larger peak between 1500 and 1600.

Our results for this location are similar across the three simulated years matching the studied periods, with all three sets of results displaying bimodal distributions of dust devil lifting. The results envelopes for all three years show a small peak in morning lifting (consistently between 0900 and 1000) and a larger peak in afternoon lifting. Our Year 1 results are not a good match for the study's season 1 results: our results lack the near mid-sol peak of the study observations, although Greeley et al. (2010) did identify dust devils during both the morning and afternoon periods of our results envelope. Year 2 more closely matches the Greeley et al. (2010) season 2 results, with a broader afternoon peak spanning 1300 to 1600, while observations peaked between 1400 and 1500. Our Year 3 results again lack the mid-sol lifting evident in the season 3 observations, but the timing of the afternoon peak shows a good match between results and observations.

Kahanpää et al. (2016) identified 252 likely convective vortices in MSL Curiosity pressure data recorded during the first full year of operations, 668 sols from L_S = 157° MY31 to L_S =157° MY32. Maximum vortex activity was observed between 1100 and 1300. Our results for this location show a strong bimodal distribution of lifting, with activity peaking at 1100 and 1500 (Figure 4d). The morning peak is an hour earlier than the observed peak in activity, but is similar in profile. The peak in afternoon activity is not evident in the observations, although vortices were detected in the afternoon. (For

completeness, we also considered the vortex activity at Gale crater reported by Steakley and Murphy (2016). Those authors identified a similar peak in vortex numbers between 1100 and 1300, reporting 245 vortices during the first 707 sols of the mission. We consider their results a close enough match to those of Kahanpää et al. (2016) that we will use only the latter for comparison.)

The comparison between our results and the various lander/rover study results does not always give a good match, but there are several caveats to note: (i) the resolution at which the simulation was completed results in gridboxes that cover several hundred square kilometres in area. The data produced in such a simulation relate to quantities present in these large-scale gridboxes, not at specific local points upon the surface. The

Lander site	MGCM results	Observation results	Comment on match
VL2	Strong afternoon peak (1700)	Strong peak 1000-1100, second peak 1500-1600	Partial match: morning lifting present but limited, afternoon lifting late
Pathfinder	Strong afternoon peak (1400)	Strong peak 1200-1300	Good match in shape of distribution, timing similar
Phoenix	Broad span, sharp peak around 1600	Broad span, peaking 1300-1400	Good match to timing of distribution
MER Spirit	Morning and afternoon peaks	Peak spanning mid-sol	Minimal match: mid-sol peak not seen
		Mid-afternoon peak 1400-1500	Good match: afternoon lifting encompasses most observations
		Mid-sol lifting, afternoon peak 1500-1600	Partial match: mid-sol peak not seen but afternoon peak matches observations
MSL Curiosity	Late morning (1100) and mid-afternoon (1500) peaks	Strong peak 1100-1200	Partial match: morning peak early, afternoon lifting greater than observed

Table 2: Summary of MGCM dust devil lifting results and dust devil observations from the comparison studies, with comment on the match of results to observations.

locations used in the above comparisons provide the closest possible correlation to the lander/rover sites; (ii) the studies that use pressure data can clearly detect vortices, but not all vortices necessarily entrain dust; (iii) the studies that rely on image data are limited to a certain field of view (for example, rover camera pointing) and often restricted in the times at which images were taken (e.g. 1300-1500 for MOC images); and (iv) although our model provides a calculation for the rate of dust lifting by dust devils, our data contain no information on either the number or the size of the dust devils required to lift such an amount of dust. Within this work we have made the assumption that all Martian dust devils are similar in their dust lifting efficiency; i.e. the presence of more dust devils will result in more dust being lifted, allowing a direct comparison between the number of vortices recorded and the amount of lifted dust.

4.3. Alternative simulations

Figures 1 to 3 show results from a simulation that used a relatively low atmospheric dust loading. In order to check whether our results were specific only to low dust cases, an additional simulation was completed that utilised a higher atmospheric dust loading (corresponding to the higher levels of atmospheric dust loading observed during MY25). The results of this simulation produce similar histogram curves to those presented in Figure 3: peak dust devil lifting occurs during both the morning and the afternoon across the globe during the Northern Hemisphere spring and summer months, shifting to afternoon-dominated lifting during the months approaching and retreating from perihelion. Figure 14 shows this shift away from morning lifting occurring slightly earlier in the year in this simulation than in the lower atmospheric dust simulation: the 'southern summer' afternoon peak in dust devil lifting begins around $L_S = 180°$.

The simulations discussed so far were completed at a resolution typical of global climate modelling: 5° latitude × 5° longitude. This results in a physical scale that is too large to capture local variations in surface properties, particularly with regard to small-scale topographical variability. In order to begin investigating the effect of simulation resolution on these results, a simulation was completed at a model resolution that corresponds to a physical resolution of 3.75° latitude × 3.75° longitude. The results of this simulation are again similar to those presented in Figure 3.

It should be noted that this higher resolution simulation will still not fully capture very local surface variations. For example, near-surface wind flows will be influenced by topographical forcing associated with craters that are beyond the resolution of our simulations. However, these resolutions are commonly used to investigate a number of atmospheric processes, and our results remain pertinent to those investigations, even if very local effects cannot be resolved.

The calculation of sensible heat flux, F_s, used in the dust devil parameterisation incorporates the surface drag coefficient, C_D, which in turn depends on the surface roughness length z_0. The value of z_0 was set to the 'standard' value of 1 cm for the simulations above. To check whether this simplification had any effect on the diurnal frequency distribution of dust devil activity, a comparison simulation was performed using a surface roughness map derived from rock abundance data (as described in Hébrard et al. (2012)). Using a value of z_0 that varies across the planet's surface does affect the amount of dust lifted by dust devils, but the bimodal distribution is still observed in the resulting time-of-sol histograms.

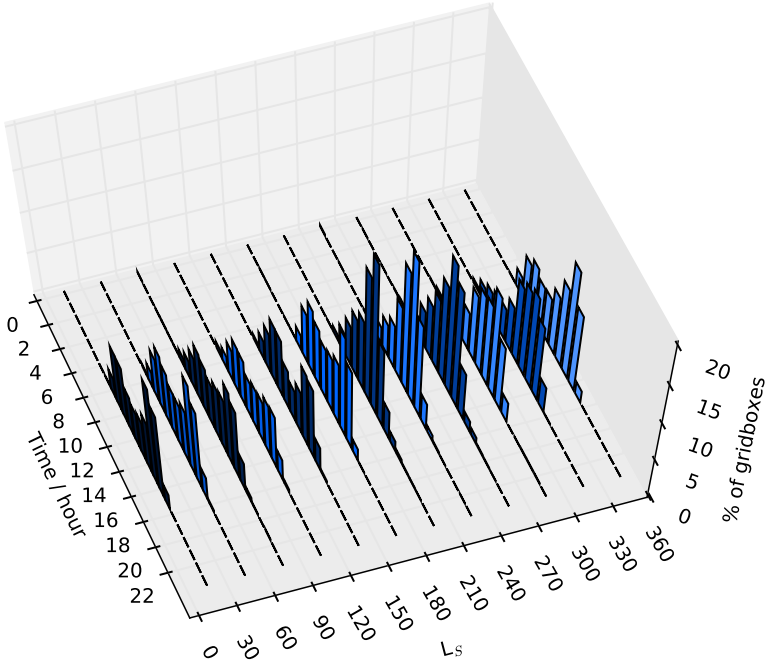

Figure 14: As Figure 3, but displaying data from a simulation using a higher atmospheric dust loading (corresponding to MY25, in which a global dust storm occurred). A bimodal distribution in peak dust devil lifting timing is visible for the sections spanning L_S = 0-180° and L_S = 330-360° (Northern Hemisphere spring and summer), while the sections spanning L_S = 180-330° (Northern Hemisphere autumn and winter) display a unimodal distribution.

5. Summary

Parameterised dust devil activity depends on the sensible heat available to the dust devil and its thermodynamic efficiency (how readily it converts available heat into work). The thermodynamic efficiency of a dust devil is driven by the depth of the local CBL, which follows a predictable diurnal pattern driven by atmospheric heating due to insolation. Most of the parameters used to calculate the sensible heat flux also follow predictable diurnal patterns, the exception being the near-surface wind speed, which is more stochastic in nature. It is this variability within the near-surface wind speed that introduces variability into the diurnal timings of dust devils. The dust devil parameterisation in operation within the MGCM has been used as the basis for similar parameterisations in the NASA Ames Mars GCM and the GFDL Mars GCM.

Our results show that, within MGCM simulations, more dust is lifted by dust devils during morning hours than was previously anticipated. This disparity is primarily due to the fact that most assumptions made about the diurnal variation of Martian dust devils have (necessarily) been based upon observations of terrestrial dust devils. Our results suggest two possible conclusions: that dust devil parameterisations developed for use in MGCMs do not correctly represent diurnal dust devil behaviour, or that the generally

accepted description of dust devil behaviour on Mars (i.e. that dust devil activity follows a unimodal distribution that peaks around mid-sol or later) is not complete.

Comparing our results with those of the studies reporting surface observations, it appears that the MGCM dust devil parameterisation does reasonably represent observed dust devil diurnal behaviour in the vicinities of the lander locations. For these studies, which comprise the majority of surface-based dust devil studies that discuss diurnal timings, three of the comparisons show a good match between our results and the observations, three show a partial match, and one shows a minimal match (counting each of the three seasons in Greeley et al. (2010) as a separate comparison). All of these comparison studies observed dust devils (or pressure vortices) during morning hours, and a range is seen in the timings of the data maxima across studies.

Studies that include diurnal surveys of dust devils using orbital observations have not identified a large number of dust devils during morning hours. These studies are few in number, probably due to the fact that many orbital observations are temporally restricted by spacecraft positioning (Fisher et al., 2005; Cantor et al., 2006), and therefore contain little information on diurnal variability. The published diurnal distribution of dust devils observed from orbit is not a good match to the majority of surface observations. As noted in Section 4.2, orbital observations are biased towards capturing large dust devils, and thus may not correctly represent the true dust devil population (Stanzel et al., 2008).

Our results agree with a majority of published surveys, and disagree with the assumption that Martian dust devil timing distributions can be simply extrapolated from terrestrial observations. Dust devil activity will not necessarily peak in the early afternoon, and local wind speeds may act as a strong governor of the timings of dust devils. We suggest that the generally accepted description of dust devil behaviour on Mars is incomplete.

Theories of dust devil formation may need to be further developed (or specifically tailored) in order to be truly applicable to vortices forming in a thin atmosphere over a desert that covers the entire surface of a planet. Lorenz and Radebaugh (2016) suggest that dust devils are "systematically more common" within low pressure environments. Ringrose et al. (2003) identify the possibility that Martian dust devils form earlier in the sol than terrestrial dust devils due to the lower dry adiabatic lapse rate within the Martian atmosphere; this complements the analysis of terrestrial dust devils by Jemmett-Smith et al. (2015), in which a modelled lower lapse rate resulted in a wider diurnal range of potential dust lifting activity.

While dust devil theories may not transfer directly between terrestrial and Martian dust devils, the parameterisation may also need improvement. One factor that must be considered is that of the input heat source driving the model dust devil 'heat engine'. On Earth the sensible heat flux is a large factor in the total surface energy budget (Larsen et al., 2002), but on Mars the surface energy budget calculation is dominated by radiative fluxes, due to the lower density of the Martian atmosphere (Petrosyan et al., 2011). Terrestrial models of dust devils use the sensible heat flux as the dominant heat source driving their formation (e.g. Koch and Rennó (2005)); it is possible that the MGCM dust devil parameterisation should incorporate a more complex representation of the heat available for dust devil formation at the Martian surface-atmosphere boundary. A good test of the current dust devil parameterisation would be to incorporate it into a terrestrial GCM: the existing sensible heat flux formulation could be expected to produce results that are a good match for terrestrial dust devil activity (within the limited dusty

areas on Earth).

To support development of theories of Martian dust devil formation and behaviour, further surveys of dust devil observations are required. These observations should encompass the full diurnal period. Martian dust devil observations should also be considered within a wider meteorological context, in order to enable investigation of connections between dust devils and local meteorological conditions, and allow subsequent comparison with similar studies of terrestrial dust devils (e.g. Balme et al. (2012)).

A near-future surface mission that may facilitate such observations is NASA's InSight (planned to carry temperature, pressure and wind sensors, and cameras (Smrekar, 2015)). Orbital images that span the diurnal period may be obtained from the Colour and Stereo Surface Imaging System (CaSSIS) instrument (Roloff et al., 2015) carried aboard ESA's ExoMars Trace Gas Orbiter.

6. Conclusions

In this paper we have presented the results of our investigation into the diurnal variation of dust devil activity, discussed the details of the MGCM dust devil parameterisation, and compared our results with lander and spacecraft observations. In conclusion:

- The modelled dust devil activity displays a wider than anticipated diurnal range, with more activity occurring during the morning than was expected. Heating due to insolation produces conditions suitable for dust devil formation, but we identify that the diurnal variability of dust devil activity is governed by local wind speeds: higher wind speeds generate higher levels of dust devil activity.

- Our results show a good match with a number of studies reporting on surface observations of Martian dust devils, in which landers have observed a range of dust lifting diurnal distributions. We do not find a good match between our results and global surveys of Martian dust devils conducted using images obtained from orbit. However, orbital dust devil surveys are often temporally limited by spacecraft pointing restrictions.

- Theories of terrestrial dust devil formation may need to be further developed, or tailored more specifically, in order to better fit the Martian environment. More surveys of Martian dust devils are required to support this development: orbital surveys that include observations encompassing the full diurnal cycle, and surface observations that can be placed within a wider meteorological context, including local temperatures and wind speeds.

Acknowledgements

The authors thank the UK Space Agency for funding under grant ST/M00306X/1 and the UK Science and Technology Facilities Council for funding under grant ST/L000776/1. The authors would also like to thank two anonymous reviewers for their comments, which have helped us to improve this paper.

References

Balme, M. R., Hagermann, A., 2006. Particle lifting at the soil-air interface by atmospheric pressure excursions in dust devils. Geophys. Res. Lett. 33 (19), L19S01.

Balme, M. R., Metzger, S. M., Towner, M. C., Ringrose, T. J., Greeley, R., Iversen, J., 2003a. Friction wind speeds in dust devils: A field study. Geophys. Res. Lett. 30 (16).

Balme, M. R., Pathare, A., Metzger, S. M., Towner, M. C., Lewis, S. R., Spiga, A., Fenton, L. K., Renno, N. O., Elliott, H. M., Saca, F. A., Michaels, T. I., Russell, P., Verdasca, J., 2012. Field measurements of horizontal forward motion velocities of terrestrial dust devils: Towards a proxy for ambient winds on Mars and Earth. Icarus 221 (2), 632–645.

Balme, M. R., Whelley, P. L., Greeley, R., 2003b. Mars: Dust devil track survey in Argyre Planitia and Hellas Basin. J. Geophys. Res. Planets 108 (E8), 5086.

Basu, S., Richardson, M. I., Wilson, R. J., 2004. Simulation of the Martian dust cycle with the GFDL Mars GCM. J. Geophys. Res. 109 (E11), E11006.

Basu, S., Wilson, J., Richardson, M. I., Ingersoll, A., 2006. Simulation of spontaneous and variable global dust storms with the GFDL Mars GCM. J. Geophys. Res. 111 (9), E09004.

Cantor, B. A., Kanak, K. M., Edgett, K. S., 2006. Mars Orbiter Camera observations of Martian dust devils and their tracks (September 1997 to January 2006) and evaluation of theoretical vortex models. J. Geophys. Res. 111 (E12), E12002.

Clancy, R. T., Sandor, B. J., Wolff, M. J., Christensen, P. R., Smith, M. D., Pearl, J. C., Conrath, B. J., Wilson, R. J., 2000. An intercomparison of ground-based millimeter, MGS TES, and Viking atmospheric temperature measurements: Seasonal and interannual variability of temperatures and dust loading in the global Mars atmosphere. J. Geophys. Res. 105 (E4), 9553.

Colburn, D. S., Pollack, J. B., Haberle, R. M., 1989. Diurnal variations in optical depth at Mars. Icarus 79 (1), 159–189.

Ellehoj, M. D., Gunnlaugsson, H. P., Taylor, P. A., Kahanpää, H., Bean, K. M., Cantor, B. A., Gheynani, B. T., Drube, L., Fisher, D., Harri, A.-M., Holstein-Rathlou, C., Lemmon, M. T., Madsen, M. B., Malin, M. C., Polkko, J., Smith, P. H., Tamppari, L. K., Weng, W., Whiteway, J. A., 2010. Convective vortices and dust devils at the Phoenix Mars mission landing site. J. Geophys. Res. 115, E00E16.

Esau, I. N., 2004. Parameterization of a surface drag coefficient in conventionally neutral planetary boundary layer. Ann. Geophys. 22, 3353–3362.

Ferri, F., Smith, P. H., Lemmon, M. T., Renno, N. O., 2003. Dust devils as observed by Mars Pathfinder. J. Geophys. Res. 108 (E12), 5133.

Fisher, J. A., Richardson, M. I., Newman, C. E., Szwast, M. A., Graf, C., Basu, S., Ewald, S. P., Toigo, A. D., Wilson, R. J., 2005. A survey of Martian dust devil activity using Mars Global Surveyor Mars Orbiter Camera images. J. Geophys. Res. 110 (E3), E03004.

Forget, F., Hourdin, F., Fournier, R., Hourdin, C., Talagrand, O., Collins, M., Lewis, S. R., Read, P. L., Huot, J. P., 1999. Improved general circulation models of the Martian atmosphere from the surface to above 80 km. J. Geophys. Res. 104 (E10), 24155–24175.

Greeley, R., Balme, M. R., Iversen, J., Metzger, S. M., Mickelson, R., Phoreman, J., White, B., 2003. Martian dust devils: Laboratory simulations of particle threshold. J. Geophys. Res. 108 (E5), 5041.

Greeley, R., Waller, D. A., Cabrol, N. A., Landis, G. A., Lemmon, M. T., Neakrase, L. D. V., Pendleton Hoffer, M., Thompson, S. D., Whelley, P. L., 2010. Gusev Crater, Mars: Observations of three dust devil seasons. J. Geophys. Res. 115, E00F02.

Greeley, R., Whelley, P. L., Arvidson, R. E., Cabrol, N. A., Foley, D. J., Franklin, B. J., Geissler, P. G., Golombek, M. P., Kuzmin, R. O., Landis, G. A., Lemmon, M. T., Neakrase, L. D. V., Squyres, S. W., Thompson, S. D., 2006. Active dust devils in Gusev crater, Mars: Observations from the Mars Exploration Rover Spirit. J. Geophys. Res. 111 (E12), E12S09.

Hébrard, E., Listowski, C., Coll, P., Marticorena, B., Bergametti, G., Määttänen, A., Montmessin, F., Forget, F., 2012. An aerodynamic roughness length map derived from extended Martian rock abundance data. J. Geophys. Res. Planets 117 (E04008).

Hinson, D. P., Pätzold, M., Tellmann, S., Häusler, B., Tyler, G. L., 2008. The depth of the convective boundary layer on Mars. Icarus 198 (1), 57–66.

Jemmett-Smith, B. C., Marsham, J. H., Knippertz, P., Gilkeson, C. A., 2015. Quantifying global dust devil occurrence from meteorological analyses. Geophys. Res. Lett. 42 (4), 1275–1282.

Kahanpää, H., Newman, C. E., Moores, J., Zorzano, M.-P., Martín-Torres, J., Navarro, S., Lepinette, A., Cantor, B. A., Lemmon, M. T., Valentín-Serrano, P., Ullán, A., Schmidt, W., 2016. Convective vortices and dust devils at the MSL landing site: Annual variability. J. Geophys. Res. Planets.

Kahre, M. A., Hollingsworth, J. L., Haberle, R. M., Murphy, J. R., 2008. Investigations of the variability

of dust particle sizes in the martian atmosphere using the NASA Ames General Circulation Model. Icarus 195 (2), 576–597.
Kahre, M. A., Murphy, J. R., Haberle, R. M., 2006. Modeling the Martian dust cycle and surface dust reservoirs with the NASA Ames general circulation model. J. Geophys. Res. 111 (E6), E06008.
Koch, J., Rennó, N. O., 2005. The role of convective plumes and vortices on the global aerosol budget. Geophys. Res. Lett. 32 (18).
Kurgansky, M. V., Montecinos, A., Villagran, V., Metzger, S. M., 2010. Micrometeorological conditions for dust-devil occurrence in the Atacama Desert. Boundary-Layer Meteorol. 138 (2), 285–298.
Larsen, S. E., Jørgensen, H. E., Landberg, L., Tillman, J. E., 2002. Aspects of the atmospheric surface layers on Mars and Earth. Boundary-Layer Meteorol. 105, 451–470.
Lewis, S. R., Collins, M., Read, P. L., Forget, F., Hourdin, F., Fournier, R., Hourdin, C., Talagrand, O., Huot, J. P., 1999. A climate database for Mars. J. Geophys. Res. 104 (E10), 24177.
Lorenz, R. D., Lanagan, P. D., 2014. A barometric survey of dust-devil vortices on a desert playa. Boundary-Layer Meteorol. 153 (3), 555–568.
Lorenz, R. D., Radebaugh, J., 2016. Dust devils in thin air: Vortex observations at a high elevation Mars analog site in the Argentinian Puna. Geophys. Res. Lett.
Lyons, T. J., Nair, U. S., Foster, I. J., 2008. Clearing enhances dust devil formation. J. Arid Environ. 72 (10), 1918–1928.
Martin, T. Z., 1986. Thermal infrared opacity of the Mars atmosphere. Icarus 66 (1), 2–21.
Montabone, L., Forget, F., Millour, E., Wilson, R. J., Lewis, S. R., Cantor, B. A., Kass, D., Kleinböhl, A., Lemmon, M. T., Smith, M. D., Wolff, M. J., 2015. Eight-year climatology of dust optical depth on Mars. Icarus 251, 65–95.
Mulholland, D. P., 2012. Martian dust lifting, transport and associated processes. Ph.D. thesis, St. Anne's College, University of Oxford.
Mulholland, D. P., Read, P. L., Lewis, S. R., 2013. Simulating the interannual variability of major dust storms on Mars using variable lifting thresholds. Icarus 223 (1), 344–358.
Murphy, J. R., Nelli, S., 2002. Mars Pathfinder convective vortices: Frequency of occurrence. Geophys. Res. Lett. 29 (23), 2103.
Newman, C. E., Lewis, S. R., Read, P. L., Forget, F., 2002. Modeling the Martian dust cycle 1. Representations of dust transport processes. J. Geophys. Res. 107 (E12), 5123.
Oke, A. M. C., Tapper, N. J., Dunkerley, D., 2007. Willy-willies in the Australian landscape: The role of key meteorological variables and surface conditions in defining frequency and spatial characteristics. J. Arid Environ. 71 (2), 201–215.
Petrosyan, A., Galperin, B., Larsen, S. E., Lewis, S. R., Määttänen, A., Read, P. L., Rennó, N. O., Rogberg, L. P. H. T., Savijärvi, H., Siili, T., Spiga, A., Toigo, A. D., Vázquez, L., 2011. The Martian atmospheric boundary layer. Rev. Geophys. 49 (3), RG3005.
Pollack, J. B., Colburn, D. S., Kahn, R., Hunter, J., Van Camp, W., Carlston, C. E., Wolf, M. R., 1977. Properties of aerosols in the Martian atmosphere, as inferred from Viking Lander imaging data. J. Geophys. Res. 82 (28), 4479–4496.
Read, P. L., Lewis, S. R., 2004. The Martian Climate Revisited. Springer, Praxis Publishing.
Reiss, D., Spiga, A., Erkeling, G., 2014. The horizontal motion of dust devils on Mars derived from CRISM and CTX/HiRISE observations. Icarus 227, 8–20.
Rennó, N. O., Burkett, M. L., Larkin, M. P., 1998. A simple thermodynamical theory for dust devils. J. Atmos. Sci. 55 (21), 3244–3252.
Ringrose, T. J., Towner, M. C., Zarnecki, J. C., 2003. Convective vortices on Mars: a reanalysis of Viking Lander 2 meteorological data, sols 1–60. Icarus 163 (1), 78–87.
Roloff, V., Gambicorti, L., Pommerol, A., Thomas, N., 2015. Scientific calibration and analysis of calibration data for the CaSSIS instrument of the ExoMars Trace Gas Orbiter. In: Eur. Planet. Sci. Congr. 2015.
Sinclair, P. C., 1964. Some preliminary dust devil measurements. Mon. Weather Rev. 92 (8), 363–367.
Sinclair, P. C., 1969. General characteristics of dust devils. J. Appl. Meteorol. 8 (1), 32–45.
Smith, M. D., Pearl, J. C., Conrath, B. J., Christensen, P. R., 2001. Thermal Emission Spectrometer results: Mars atmospheric thermal structure and aerosol distribution. J. Geophys. Res. 106 (E10), 23929.
Smith, P. H., Lemmon, M. T., 1999. Opacity of the Martian atmosphere measured by the Imager for Mars Pathfinder. J. Geophys. Res. 104 (E4), 8975.
Smrekar, S., 2015. The InSight mission's Martian atmospheric science goals, capabilities and instrumentation. In: 2015 AGU Fall Meet. AGU.
Snow, J. T., McClelland, T. M., 1990. Dust devils at White Sands Missile Range, New Mexico: 1.

Temporal and spatial distributions. J. Geophys. Res. 95 (D9), 13707.
Spiga, A., Forget, F., Lewis, S. R., Hinson, D. P., 2010. Structure and dynamics of the convective boundary layer on Mars as inferred from large-eddy simulations and remote-sensing measurements. Q. J. R. Meteorol. Soc. 136, 414–428.
Stanzel, C., Pätzold, M., Greeley, R., Hauber, E., Neukum, G., 2006. Dust devils on Mars observed by the High Resolution Stereo Camera. Geophys. Res. Lett. 33 (11), L11202.
Stanzel, C., Pätzold, M., Williams, D., Whelley, P. L., Greeley, R., Neukum, G., 2008. Dust devil speeds, directions of motion and general characteristics observed by the Mars Express High Resolution Stereo Camera. Icarus 197 (1), 39–51.
Steakley, K., Murphy, J. R., 2016. A year of convective vortex activity at Gale Crater. Icarus.
Strausberg, M. J., Wang, H., Richardson, M. I., Ewald, S. P., Toigo, A. D., 2005. Observations of the initiation and evolution of the 2001 Mars global dust storm. J. Geophys. Res. 110 (E2), E02006.
Thomas, P., Gierasch, P. J., 1985. Dust devils on Mars. Science (80-.). 230 (4722), 175–7.
Toigo, A. D., Richardson, M. I., 2003. Meteorology of proposed Mars Exploration Rover landing sites. J. Geophys. Res. 108 (E12), 8092.
Toigo, A. D., Richardson, M. I., Ewald, S. P., Gierasch, P. J., 2003. Numerical simulation of Martian dust devils. J. Geophys. Res. 108 (E6), 5047.
Wilson, R. J., 2011. Dust cycle modeling with the GFDL Mars General Circulation Model. In: Fourth Int. Work. Mars Atmos. Model. Obs.
Wilson, R. J., Hamilton, K., 1996. Comprehensive Model Simulation of Thermal Tides in the Martian Atmosphere. J. Atmos. Sci. 53 (9), 1290–1325.
Zurek, R. W., 1978. Solar heating of the Martian dusty atmosphere. Icarus 35 (2), 196–208.